Fast Strain Mapping of Nanowire Light-Emitting Diodes Using Nanofocused X-ray Beams

Tomaš Stankevič,[*,†] Emelie Hilner,[†] Frank Seiboth,[‡] Rafal Ciechonski,[§] Giuliano Vescovi,[§] Olga Kryliouk,[⊥] Ulf Johansson,[∥] Lars Samuelson,[∥] Gerd Wellenreuther,[¶] Gerald Falkenberg,[¶] Robert Feidenhans'l,[†] and Anders Mikkelsen[∥]

[†]Niels Bohr Institute, University of Copenhagen, Universitetsparken 5, 2100 Copenhagen, Denmark, [‡]Technische Universität Dresden, D-01062 Dresden, Germany, [§]Glo AB, Scheelevägen 17, Betahuset 6, 223 70 Lund, Sweden, [⊥]Glo-USA, Inc., 1225 Bordeaux Drive, Sunnyvale, California 94089, United States, [∥]Lund University, 22100 Lund, Sweden, and [¶]Deutsches Elektronen-Synchrotron DESY, Notkestrasse 85, D-22607 Hamburg, Germany

ABSTRACT X-ray nanobeams are unique nondestructive probes that allow direct measurements of the nanoscale strain distribution and composition inside the micrometer thick layered structures that are found in most electronic device architectures. However, the method is usually extremely time-consuming, and as a result, data sets are often constrained to a few or even single objects. Here we demonstrate that by special design of a nanofocused X-ray beam diffraction experiment we can (in a single 2D scan with no sample rotation) measure the individual strain and composition profiles of many structures in an array of upright standing nanowires. We make use of the observation that in the generic nanowire device configuration, which is found in high-speed transistors, solar cells, and light-emitting diodes, each wire exhibits very small degrees of random tilts and twists toward the substrate. Although the tilt and twist are very small, they give a new contrast mechanism between different wires. In the present case, we image complex nanowires for nanoLED fabrication and compare to theoretical simulations, demonstrating that this fast method is suitable for real nanostructured devices.

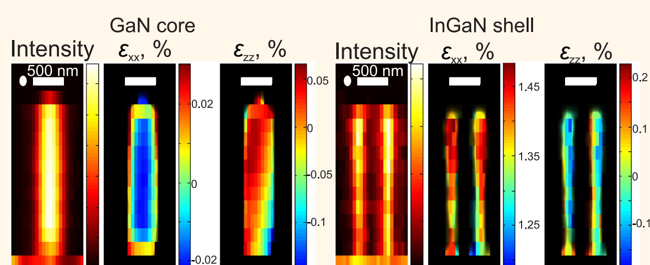

KEYWORDS: core–shell nanowires · scanning X-ray diffraction microscopy · strain mapping · nanofocused X-rays

Promising novel devices based on self-assembled nanowires such as field-effect transistors, light-emitting diodes (LEDs), and solar cells[1−7] all have a number of generic, material-independent design features in common: the fundamental component consists of a nanowire core surrounded by a number of shells with varying composition and structure. Core–shell structures function to enhance the light extraction in LEDs, absorption in solar cells,[8,9] and field control in transistors, dramatically improving device performance. However, the creation of layer-upon-layer in the core–shell configuration will introduce strain and compositional variations that are different from what is observed in planar structures. That has a direct impact on the electronic/photonic properties of the devices but can also be intentionally used to fine-tune the band structure.[10,11] Although a number of methods to characterize individual NWs have been developed, most of them require destructive sample preparation.[12,13] Electron-microscopy-based techniques can only probe samples up to 200 nm thick; therefore, micrometer thick devices have to be sliced. Only nanofocused X-ray beams allow for nondestructive direct measurement of strain, composition,[14−22] and crystal defects[23,24] inside such structures.

Changes of strain and composition in a sample can be viewed as areas of different lattice constants, which are directly related to a scattering angle *via* Bragg's law. In the case of three-dimensional strain distributions, which are present in core–shell nanowires, some parts of the sample have to be oriented at different angles with respect to the incident X-rays to satisfy the Bragg condition. Therefore, the standard assumption has been that the sample must be rotated in order to get a complete picture of the strain distribution. The disadvantage of such

* Address correspondence to tomas.stankevic@nbi.dk.

Received for review February 27, 2015 and accepted June 19, 2015.

Published online June 19, 2015
10.1021/acsnano.5b01291

© 2015 American Chemical Society

a technique is that the sample rotation combined with 2D scanning leads to very long measurement times.

Often, nanowires are slightly tilted with respect to each other. This is especially true for the core–shell nanowires which exhibit spontaneous bending under strong axial stresses caused by the lattice mismatch between the core and the shell.[25,26] Even the slightest asymmetry in composition or thickness between two sides of the NW leads to the noticeable bending. If each of the nanostructures on a sample is tilted slightly differently with respect to the substrate, the diffraction patterns will also be shifted, allowing us to separate out several wires illuminated in the same X-ray beam. Thus, when scanning across the sample containing multiple NWs, each of them has slightly different orientation with respect to the incoming X-ray beam, and the Bragg condition is satisfied for different sets of crystal planes and ranges of lattice constants depending on where the X-ray beam will hit on the sample. In this way, different parts of the nanowires can be selected by scanning from one to another, and the homogeneity of the individual nanowires can be visualized. Clearly, if too many wires are illuminated at the same time, it will no longer be possible to distinguish the different wires. Further, there will be a trade-off between the detailed imaging of each diffraction spot to get strain and composition on one side and the imaging of a sufficiently large set of diffraction spots in reciprocal space to allow solid identification of the nanowires on the other side. Here we show that a sweet-spot exists for an experimental setup to fulfill all of these requirements.

In the present case, the nanowires are randomly tilted about ±0.2°, which is a moderate tilt compared to other, thinner or more lattice-mismatched core–shell nanowires.[25,27] If a random tilt within ±0.2° is assumed and the width of the Bragg is 0.1°, only 1/4 NWs will be in the Bragg condition for a given reflection. Moreover, they will be spread along the Debye-Scherer cone, and 2–3 smaller peaks can be separated on the detector. Thus, along the line of sight of the X-ray beam, a single NW can be analyzed separately from the rest along this line for up to 10 NWs. When higher order Bragg peaks are measured, this number can be even larger.

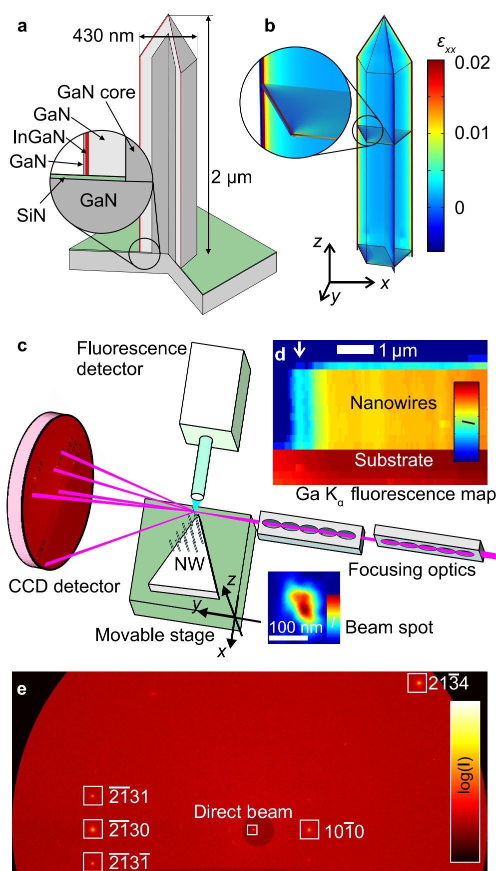

Figure 1. Experiment setup and measurement results. (a) Sketch of a NW showing the onion-like structure. (b) Finite element method simulation of strain distribution. (c) Nano-focused X-ray beam setup for diffraction mapping. (d) Gallium fluorescence map of the scan. A single nanowire at the edge of the forest is indicated with an arrow. (e) Part of the charge-coupled device image, where five Bragg peaks and the attenuated direct beam are visible. A video showing changes of the detector image during the scan is available in the Supporting Information.

RESULTS AND DISCUSSION

The measurements were done on blue (428 nm) light-emitting GaN/InGaN quantum well (QW) core–shell nanowire structures, which were grown at GLO AB by selective area metal–organic chemical vapor deposition (MOCVD) on 4 μm thick GaN (0001) films grown on sapphire substrates. The final nanostructures, as shown in Figure 1a, consisted of an axially grown GaN core, a radially grown GaN core, a 5 nm thick InGaN QW with around 8% In, and a GaN quantum barrier (QB). In order to focus on the individual nanowires, the sample was cleaved to create a sharp 60° corner with a few isolated nanowires at the tip (see Figure 1c). After the sample was cleaved, all the NWs were left intact.

The experiment was conducted at a setup consisting of nanofocusing optics, a movable sample stage, and detectors for fluorescence and diffraction signals, as shown in Figure 1c. The sample was brought into the focus of the 80 × 100 nm^2 X-ray beam with a photon energy of 24.3 keV and was scanned in the x and z directions with 50 and 200 nm steps, respectively, while measuring the diffraction pattern with the charge-coupled device (CCD) detector. With the incoming X-ray flux of 2 × 10^7 photons per second, the exposure at each position was 10 s. The scan of 90 × 15 points took about 4 h. This time will decrease in the future when the stronger nanofocused X-ray sources become available. Relatively high photon energy resulted in a large radius of the Ewald sphere, allowing us to see more than one Bragg peak at once. The detector was positioned close enough that Bragg peaks from several

different plane families would be visible while still being able to resolve the details within individual Bragg peaks (*i.e.*, GaN and InGaN). A representative image is shown in Figure 1e, where five of the strongest Bragg peaks are labeled. The Bragg peaks within the scope of this article are noted using the four-index Miller–Bravais notation (*hkil*) common for hexagonal structures. From the known NW density on the substrate, we expect that we typically illuminate 1–10 NWs simultaneously, but due to their inhomogeneity, we can single them out one by one.

Ensemble Strain Maps. The scattered intensities in the form of Bragg peaks are directly related to the atomic positions in the sample; therefore, we can map regions of uniform crystal structure by measuring the intensities of the particular points on the detector. When an inhomogeneous crystalline material, such as a forest of nanowires, is illuminated with a nanosized beam, the Bragg peaks at a given beam position consist of multiple smaller peaks, as shown in the inset of Figure 2a. The peaks are displaced slightly from each other because some of them come from different parts of the NWs; others are shifted due to the different tilt of the individual NWs. The detailed pattern of the Bragg peak changes as a function of position of the X-ray beam depending on the local structure. Having measured such Bragg peaks at each position on the sample, we can choose a region in reciprocal space, thus selecting a range of lattice constants as narrow as 0.15% (limited by the pixel size) and visualize its distribution across the sample. Such a map is shown in Figure 2a, where four different colors represent regions of the measured intensities indicated with the corresponding arrows on the Bragg peaks. The color saturation is proportional to the intensity of the given pixels. For example, the blue feature that corresponds to the GaN core of the nanowire comes from the strongest region of the ($\bar{2}131$) peak shown with the blue arrow. On the other hand, the two green vertical stripes originate from a different position of the diffraction spot and show two sides of the InGaN QW of another NW.

The average strain in a small volume illuminated by the nanofocused beam can be found from the corresponding position of the Bragg peak on the detector. The latter can be determined with subpixel precision by calculating the center of mass of the intensity (centroid) of the isolated peaks. The tilt of the nanowires can be calculated by measuring azimuthal movement of the symmetric Bragg peaks, such as ($\bar{2}130$) and ($10\bar{1}0$). From Figure 2b, we can see that individual nanowires exhibit uniform tilt with respect to the substrate within ±0.2°. We can see that a rapid change of tilt occurs at the interface between the NWs and the substrate, whereas the tilt is constant within the single nanowires. Next, in Figure 2c, we can see the in-plane strain map calculated from the lateral movement of the ($10\bar{1}0$) Bragg peak with respect to the substrate peak. Here, due to different twisting (rotation

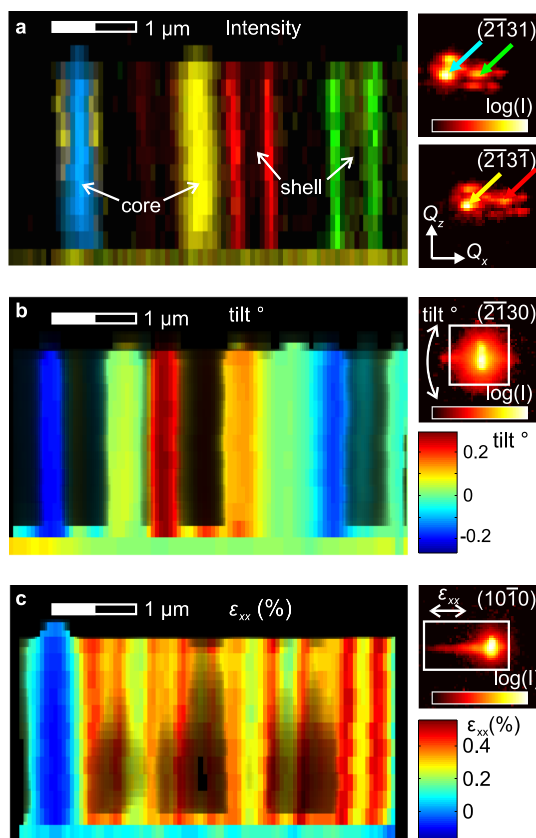

Figure 2. Intensity, tilt, and strain maps obtained from the single scan. (a) Diffraction map made using intensities of different regions of the Bragg peaks indicated with corresponding arrows. The saturation of each color is proportional to the intensity of the diffraction signal, and colors indicate the corresponding region on the diffraction spot. (b) Map of the crystal tilt of the small forest of NWs. We can see that the NWs exhibit random tilting with respect to the substrate of around 0.2°. (c) In-plane strain map calculated from the peak positions. All three maps above show results of the same scan of the sample. Videos showing how different parts of the Bragg peaks correspond to different parts of the NWs are available in Supporting Information.

around the substrate normal) of the NWs, the Bragg condition is satisfied for the core of the leftmost NW (blue), whereas the outer In-enriched layers are visible in the remaining NWs to the right, hence the contrast. Compression strain present in the core of the leftmost NW fully relaxes toward the sides where, as can be seen from the NWs to the right, tensile strain of 0.4% takes over. In Figure 2c, we selected a large region of interest (ROI), containing signals from both GaN and InGaN in order to obtain a general picture. When the beam points at the InGaN shell, some of it still illuminates the GaN core, so both peaks are present on the detector at the same time. The centroid of such ROI is biased by the stronger GaN peak, so measured strain in InGaN is lower. In the following paragraphs, we analyzed positions of the InGaN peaks separately, which give actual strain values in the shell. In this paper, we refer to ε_{xx} and ε_{zz} as relative changes in measured lattice constants $\Delta a/a$ and $\Delta c/c$ irrespective of their origin

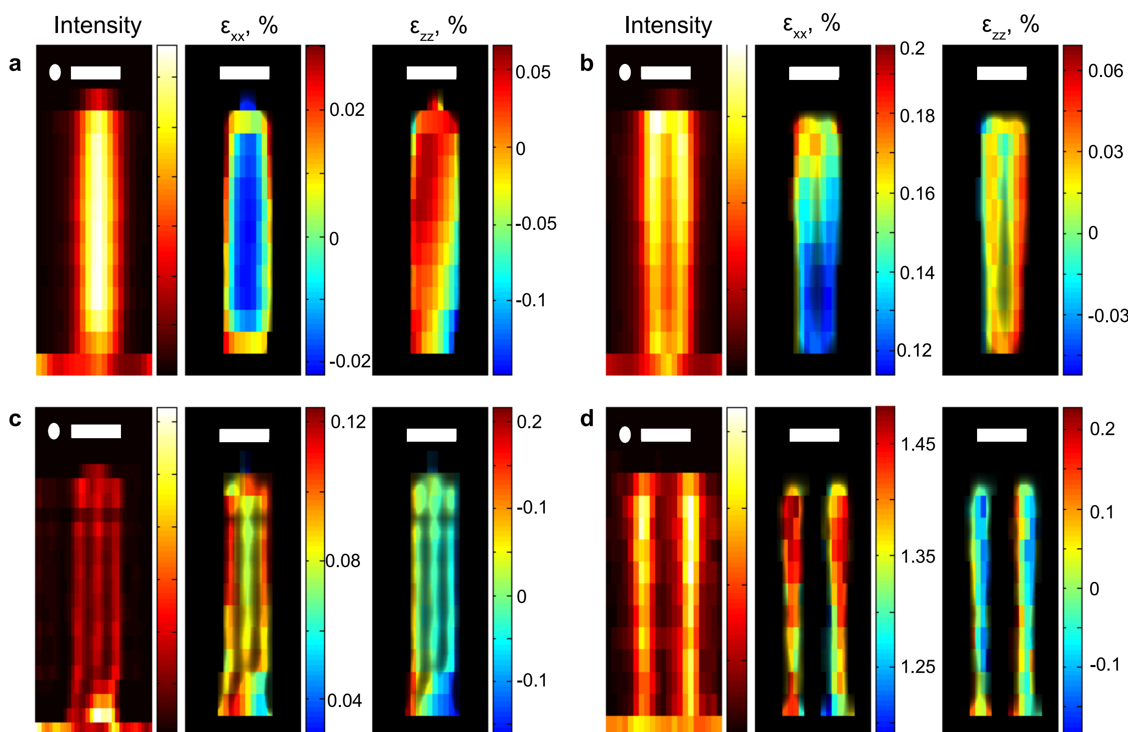

Figure 3. Four different intensity and strain projections mapped by taking the intensities of ($\bar{1}$231) and ($\bar{1}$23$\bar{1}$) Bragg peaks and the corresponding strain maps: the axially grown core (a), the radially grown core (b), the edges (c), and the shell (d). The 500 nm scale bar and full width at half-maximum of the beam spot are shown at the top of each figure.

(*i.e.*, composition or stresses). The GaN substrate region was used as a reference for zero strain.

Single Nanowire Strain Maps. More detailed strain maps, presented in Figure 3, were done by analyzing intensities and positions of the individual speckles of the two asymmetric peaks: (2$\bar{1}$31) and (2$\bar{1}$3$\bar{1}$). The strain maps in Figure 3 were thresholded with the corresponding intensity maps to remove the irrelevant background. Since the tilt within the nanowires is constant, in-plane strain ε_{xx} and out-of-plane strain ε_{zz} can be retrieved from the horizontal and vertical peak movements, respectively. Here we can look into four different NWs and visualize the strain distribution inside each NW. Different areas of the NWs were chosen by tuning the diffraction angle, which is set by the random twist and tilt of the individual NWs. First, the axially grown GaN core (a) is shown, where we can see tensile in-plane strain ε_{xx} at the outer layers, especially at the upper part and at the bottom of the nanowire. In the next panel (b), we can see two sides of the radially grown GaN core. We can see from ε_{xx} that the in-plane lattice constant increases toward the top of this NW. Next, in panel (c), we can see the intensity profile containing three vertical features that can be interpreted as a projection of the vertical edges. Finally, two sides of the shell are shown in (d), where we can see that the lattice constant is larger in the upper part of the InGaN QW. From the ε_{zz} in the shell, we can see that it is fully pseudomorphic with respect to the core. Taking this into account, we calculated that In concentration varies from 7.5% at the bottom to 8% at the top, as shown in the Supporting Information Figure S2. Calculations were done for seven different nanowires, showing a scatter in concentrations ranging from 4% up to 12%, while all of them had a similar gradient from bottom to top. A larger In concentration in the upper part of the nanowires is also responsible for higher strains in the upper part of the cores seen in Figure 3a,b.

Simulations. In order to underpin the interpretation of the diffraction maps, we performed simulations of the elastic strain relaxation using finite element method (FEM). We simulated the strain distribution using the finite element software Comsol Multiphysics. Linear anisotropic elastic theory was applied to the 3D model, where three different domains (core, QW, and QB) were distinguished by initial strain. An initial strain was applied to the InGaN QW based on the measurement results, assuming a pseudomorphic relation between the lattice-mismatched domains.

We calculated the intensity distributions around a Bragg peak and applied experimental constraints to simulate intensity projections. The Bragg peaks were calculated using the fast Fourier transform of the complex object function with a simulated displacement field as phase and a uniform shape function within the NW. The intensity distribution around the ($\bar{1}$230) Bragg peak was calculated for a number of (0001) slices from the NW. During the experiment, the detector image corresponds to the Ewald sphere cutting through a fixed point of the 3D Bragg peak, thus selecting a region which is measured. This region is different for different

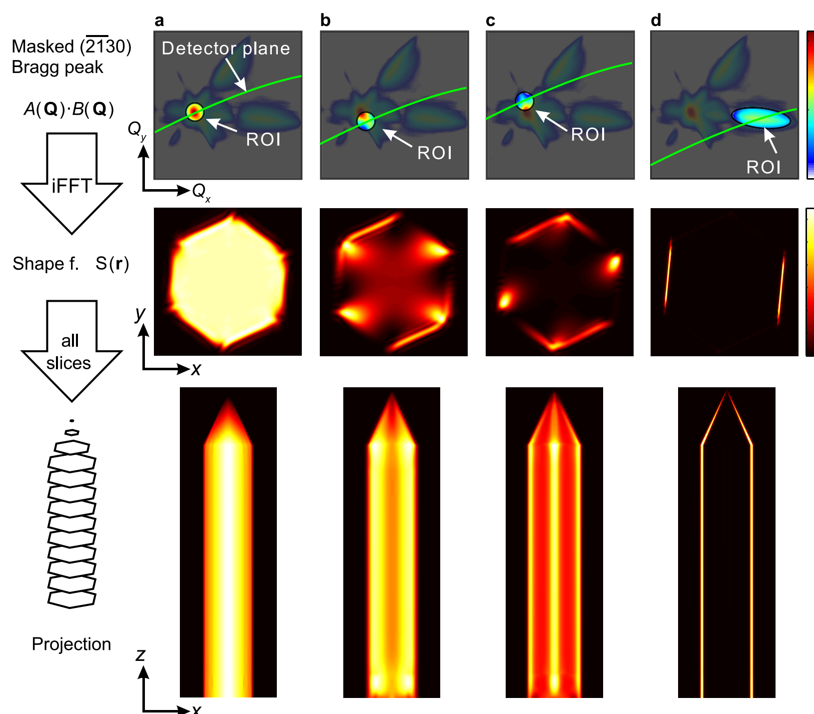

Figure 4. Simulation results showing the calculated Bragg peak *A*(Q) alongside the mask *B* choosing the ROI. The modified object shape function *S*(r) was found using the inverse Fourier transformation of the masked Bragg peak. A range of such slices were then projected on the scanning plane showing the vertical NW profile. The simulations were repeated (a−d) using four different masks *B*, creating shape function projections similar to the measured intensity profiles shown in Figure 3.

nanowires because of the random tilt and twist. Here we simulate this by choosing different regions of interest in the simulated ($\bar{1}2\bar{3}0$) Bragg peaks. A ROI (see Figure 4) was selected in reciprocal space for each slice by applying a binary mask $B(\mathbf{Q})$. The masked complex scattering wave-field was inverse Fourier transformed in order to obtain a modified object shape function $S(\mathbf{r})$. $S(\mathbf{r})$ now highlights the parts of the nanowire contributing more to the ROI in reciprocal space. Examples of such calculations are shown in Figure 4, where the simulated scattered intensity $A(\mathbf{Q})$ is shown alongside the mask selecting the ROI. Below, the calculated shape function is shown for four different ROI. A projection of the vertical nanowire on the *xz* plane is then found by combining $S_B(\mathbf{r})$ for all slices. This way, different parts of a nanowire can be isolated, such as the GaN core (Figure 4a) and the strained region in the core (Figure 4b), which creates two vertical stripes in projection similar to the ones obtained from the measurements (Figure 3b). In Figure 4c, parts around the edges of the nanowire can be identified and the projection is similar to the one in Figure 3c. Finally, by selecting the regions corresponding to the InGaN shell (Figure 4d), two sides can be isolated, showing similarity with the vertical features in Figure 3d. Inconsistencies between the measurements and simulations may result from inaccuracy of the FEM model as well as experimental errors, such as noise. For example, weaker signal coming from InGaN shell is more smeared due to the diffuse scattering from GaN.

CONCLUSION

Our results show how scanning X-ray diffraction microscopy with a nanofocused beam can be used to map the strain and composition in heterogeneous nanowires and separate different parts. Thanks to the high penetration power of X-rays, the individual nanowires can be picked separately from a small forest and imaged by relying on the structural differences. The study establishes opportunities for achieving the significant statistics that are central to performing real materials science. Local inhomogeneities were observed in the InGaN/GaN NWs, with a tendency for the larger lattice constants to be at the top part. This can be assigned to the inhomogeneous In distribution in the shell. FEM simulations of strain relaxation combined with the Fourier filtering helped to reproduce the general trend of the experimental results and identify the origin of four different intensity profiles.

METHODS

Nanowire Growth. The nanowires were grown in a close coupled showerhead reactor equipped with nitrogen precursor of NH_3 and group III precursors of trimethylgallium, triethylgallium, and trimethylindium. The GaN NWs were grown in the [0001] direction on patterned templates from the openings in

the SiN mask. The openings formed a triangular pattern with 1.5 μm spacing. The GaN NWs of the wurtzite structure were about 2 μm long and 400 nm thick. After growth of the GaN NWs, the temperature was decreased in order to grow the InGaN shell.

Scanning X-ray Diffraction Microscopy. The experiment was conducted at the nanoprobe end-station of the beamline P06 at PETRA III synchrotron radiation source (DESY, Germany). Two perpendicularly positioned nanofocusing refractive X-ray lenses (NFLs)[28] etched in the Si wafers were used to focus the 24.3 keV X-ray beam on a sample, as shown in Figure 1c. An energy-dispersive X-ray fluorescence detector was placed at 90° with respect to the beam for the sample alignment and location of the single nanowires. A 2D Mar-CCD detector with a pixel size of 80 × 80 μm was placed 10.3 cm downstream from the sample for X-ray diffraction. The size and shape of the nanofocused beam were determined using a ptychographic scan of a known test object—a pattern in a shape of a Siemens star etched in a tantalum film. Ptychography enabled the reconstruction of a complex object function and a complex illumination function of the beam simultaneously, which is routinely used for beam characterization at the beamline.[29]

Conflict of Interest: The authors declare no competing financial interest.

Acknowledgment. This work was financed from the EU-project NWs4LIGHT, Grant No. 280773, and Danish Independent Research Council *via* DANSCATT.

Supporting Information Available: Videos showing raw data, dark-field maps derived from different Bragg peaks, and additional results on the shell composition. The Supporting Information is available free of charge on the ACS Publications website at DOI: 10.1021/acsnano.5b01291.

REFERENCES AND NOTES

1. Lieber, C. M.; Wang, Z. L. Functional Nanowires. *MRS Bull.* **2011**, *32*, 99–108.
2. Garnett, E.; Yang, P. Light Trapping in Silicon Nanowire Solar Cells. *Nano Lett.* **2010**, *10*, 1082–1087.
3. Wallentin, J.; Anttu, N.; Asoli, D.; Huffman, M.; Aberg, I.; Magnusson, M. H.; Siefer, G.; Fuss-Kailuweit, P.; Dimroth, F.; Witzigmann, B.; et al. InP Nanowire Array Solar Cells Achieving 13.8% Efficiency by Exceeding the Ray Optics Limit. *Science* **2013**, *339*, 1057–1060.
4. Holm, J. V.; Jørgensen, H. I.; Krogstrup, P.; Nygård, J.; Liu, H.; Aagesen, M. Surface-Passivated GaAsP Single-Nanowire Solar Cells Exceeding 10% Efficiency Grown on Silicon. *Nat. Commun.* **2013**, *4*, 1498.
5. Dey, A. W.; Svensson, J.; Ek, M.; Lind, E.; Thelander, C.; Wernersson, L.-E. Combining Axial and Radial Nanowire Heterostructures: Radial Esaki Diodes and Tunnel Field-Effect Transistors. *Nano Lett.* **2013**, *13*, 5919–5924.
6. Hu, Y.; Churchill, H. O. H.; Reilly, D. J.; Xiang, J.; Lieber, C. M.; Marcus, C. M. A Ge/Si Heterostructure Nanowire-Based Double Quantum Dot with Integrated Charge Sensor. *Nat. Nanotechnol.* **2007**, *2*, 622–625.
7. Nadj-Perge, S.; Frolov, S. M.; Bakkers, E. P. A. M.; Kouwenhoven, L. P. Spin−Orbit Qubit in a Semiconductor Nanowire. *Nature* **2010**, *468*, 1084–1087.
8. Qian, F.; Gradecak, S.; Li, Y.; Wen, C.-Y.; Lieber, C. M. Core/Multishell Nanowire Heterostructures as Multicolor, High-Efficiency Light-Emitting Diodes. *Nano Lett.* **2005**, *5*, 2287–2291.
9. Li, S.; Waag, A. GaN Based Nanorods for Solid State Lighting. *J. Appl. Phys.* **2012**, *111*, 071101.
10. Copple, A.; Ralston, N.; Peng, X. Engineering Direct−Indirect Band Gap Transition in Wurtzite GaAs Nanowires through Size and Uniaxial Strain. *Appl. Phys. Lett.* **2012**, *100*, 193108.
11. Kadantsev, E. S.; Zieliński, M.; Hawrylak, P. Band Engineering in Nanowires: Ab Initio Model of Band Edges Modified by (111) Biaxial Strain in Group IIIA−VA Semiconductors. *Phys. Rev. B* **2012**, *86*, 085411.
12. Hytch, M.; Houdellier, F.; Hüe, F.; Snoeck, E. Nanoscale Holographic Interferometry for Strain Measurements in Electronic Devices. *Nature* **2008**, *453*, 1086–1089.
13. Moutanabbir, O.; Reiche, M.; Hähnel, A.; Erfurth, W.; Motohashi, M.; Tarun, A.; Hayazawa, N.; Kawata, S. UV-Raman Imaging of the In-Plane Strain in Single Ultrathin Strained Silicon-on-Insulator Patterned Structure. *Appl. Phys. Lett.* **2010**, *96*, 233105.
14. De Wolf, I.; Senez, V.; Balboni, R.; Armigliato, A.; Frabboni, S.; Cedola, A.; Lagomarsino, S. Techniques for Mechanical Strain Analysis in Sub-micrometer Structures: TEM/CBED, Micro-Raman Spectroscopy, X-ray Micro-diffraction and Modeling. *Microelectron. Eng.* **2003**, *70*, 425–435.
15. Hrauda, N.; Zhang, J.; Wintersberger, E.; Etzelstorfer, T.; Mandl, B.; Stangl, J.; Carbone, D.; Holý, V.; Jovanović, V.; Biasotto, C.; et al. X-ray Nanodiffraction on a Single SiGe Quantum Dot Inside a Functioning Field-Effect Transistor. *Nano Lett.* **2011**, *11*, 2875–2880.
16. Etzelstorfer, T.; Süess, M. J.; Schiefler, G. L.; Jacques, V. L. R.; Carbone, D.; Chrastina, D.; Isella, G.; Spolenak, R.; Stangl, J.; Sigg, H.; et al. Scanning X-ray Strain Microscopy of Inhomogeneously Strained Ge Micro-bridges. *J. Synchrotron Radiat.* **2014**, *21*, 111–118.
17. Gulden, J.; Mariager, S.; Mancuso, A.; Yefanov, O.; Baltser, J.; Krogstrup, P.; Patommel, J.; Burghammer, M.; Feidenhans'l, R.; Vartanyants, I. Coherent X-ray Nanodiffraction on Single GaAs Nanowires. *Phys. Status Solidi* **2011**, *208*, 2495–2498.
18. Takahashi, Y.; Suzuki, A.; Furutaku, S.; Yamauchi, K.; Kohmura, Y.; Ishikawa, T. Bragg X-ray Ptychography of a Silicon Crystal: Visualization of the Dislocation Strain Field and the Production of a Vortex Beam. *Phys. Rev. B* **2013**, *87*, 121201.
19. Holt, M. V.; Hruszkewycz, S. O.; Murray, C. E.; Holt, J. R.; Paskiewicz, D. M.; Fuoss, P. H. Strain Imaging of Nanoscale Semiconductor Heterostructures with X-ray Bragg Projection Ptychography. *Phys. Rev. Lett.* **2014**, *112*, 165502.
20. Godard, P.; Carbone, G.; Allain, M.; Mastropietro, F.; Chen, G.; Capello, L.; Diaz, A.; Metzger, T. H.; Stangl, J.; Chamard, V. Three-Dimensional High-Resolution Quantitative Microscopy of Extended Crystals. *Nat. Commun.* **2011**, *2*, 568.
21. Segura-Ruiz, J.; Martínez-Criado, G.; Denker, C.; Malindretos, J.; Rizzi, A. Phase Separation in Single $In_xGa_{1-x}N$ Nanowires Revealed through a Hard X-ray Synchrotron Nanoprobe. *Nano Lett.* **2014**, *14*, 1300–1305.
22. Biermanns, A.; Breuer, S.; Davydok, A.; Geelhaar, L.; Pietsch, U. Structural Polytypism and Residual Strain in GaAs Nanowires Grown on Si(111) Probed by Single-Nanowire X-ray Diffraction. *J. Appl. Crystallogr.* **2012**, *45*, 239–244.
23. Bussone, G.; Schäfer-Eberwein, H.; Dimakis, E.; Biermanns, A.; Carbone, D.; Tahraoui, A.; Geelhaar, L.; Haring Bolívar, P.; Schülli, T. U.; Pietsch, U. Correlation of Electrical and Structural Properties of Single As-Grown GaAs Nanowires on Si (111) Substrates. *Nano Lett.* **2015**, *15*, 981–989.
24. Keplinger, M.; Mandl, B.; Kriegner, D.; Holý, V.; Samuelsson, L.; Bauer, G.; Deppert, K.; Stangl, J. X-ray Diffraction Strain Analysis of a Single Axial $InAs_{1-x}P_x$ Nanowire Segment. *J. Synchrotron Radiat.* **2015**, *22*, 1–7.
25. Keplinger, M.; Kriegner, D.; Stangl, J.; Mårtensson, T.; Mandla, B.; Wintersberger, E.; Bauer, G. Core−Shell Nanowires: From the Ensemble to Single-Wire Characterization. *Nucl. Instrum. Methods Phys. Res., Sect. B* **2010**, *268*, 316–319.
26. Qian, F.; Li, Y.; Gradecak, S.; Park, H.-G.; Dong, Y.; Ding, Y.; Wang, Z. L.; Lieber, C. M. Multi-Quantum-Well Nanowire Heterostructures for Wavelength-Controlled Lasers. *Nat. Mater.* **2008**, *7*, 701–706.
27. Heurlin, M.; Stankevič, T.; Mickevičius, S.; Yngman, S.; Lindgren, D.; Mikkelsen, A.; Feidenhans'l, R.; Borgstrom, M. T.; Samuelson, L. Structural Properties of Wurtzite InP−InGaAs Nanowire Core−Shell Heterostructures. *Nano Lett.* **2015**, *15*, 2462–2467.
28. Schroer, C. G.; Boye, P.; Feldkamp, J. M.; Patommel, J.; Samberg, D.; Schropp, A.; Schwab, A.; Stephan, S.; Falkenberg, G.; Wellenreuther, G.; et al. Hard X-ray

Nanoprobe at Beamline P06 at PETRA III. *Nucl. Instrum. Methods Phys. Res., Sect. A* **2010**, *616*, 93–97.

29. Schroer, C. G.; Hönig, S.; Goldschmidt, A.; Hoppe, R.; Patommel, J.; Samberg, D.; Schropp, A.; Seiboth, F.; Stephan, S.; Schöder, S. Hard X-ray Nano-beam Characterization by Ptychographic Imaging. *SPIE Opt. Eng. Appl.* **2011**, 814103.